RSC Advances

PAPER

View Article Online
View Journal | View Issue

Cite this: *RSC Adv.*, 2016, **6**, 89367

Utilization of a pyrrole derivative based antimicrobial functionality impregnated onto CaO/g-C_3N_4 for dyes adsorption

Sherif A. Younis,*[ab] Ahmed Abd-Elaziz[c] and Ahmed I. Hashem[c]

Received 19th April 2016
Accepted 2nd September 2016

DOI: 10.1039/c6ra10143g

www.rsc.org/advances

A novel functionalization of CaO/g-C_3N_4 based nanocomposite using 4,5-diphenyl-2-thioxo-2,5-dihydro-1*H*-pyrrole-3-cabonitrile (P3C@CaO–HCN) was performed for wastewater remediation from organic dyes and microbial pollutants. Adsorption performance of multiple mixtures of basic and acidic dyes by P3C@CaO–HCN was investigated and optimized using a three-level Box–Behnken design of experiment (BBD-DOE). The quadratic Box–Behnken polynomial equation showed the best fit with experimental adsorption capacities of crystal violet (CV), methylene blue (MB), and methyl orange (MO) model dyes. The simultaneous influence of adsorption conditions was tested based on the developed Box–Behnken equation, 3D contour plots, and ANOVA analysis. Nonlinear regression analysis of kinetics and isotherm constants were computed and validated to propose the adsorption mechanism. Adsorption was found within the ranges of endothermic physical adsorption (ΔH° = 6.17 to 8.58 kJ mol^{-1}) and controlled by both π–π and electrostatic forces depending on the pH level in addition to film diffusion mechanism. The maximum adsorption affinity can be arranged in the order of MB > CV ≥ MO with q_e (μmol g^{-1}) of 1915.8, 1227.8, and 1221 μmol g^{-1}, respectively. At 500 mg L^{-1} P3C@CaO–HCN as the minimum inhibitory dose, the inhibition rates (*I*%) were 87.9%, 46.9%, and 72.5% for *E. coli*, *P. aeruginosa*, and *C. albicans*, respectively. The antimicrobial effect can result from the free cyanide (C≡N) functionality of a pyrrole-3-cabonitrile and protonated g-C_3N_4 (HCN) sheet, which depends on the P3C@CaO–HCN concentration and pathogen types.

1. Introduction

Many kinds of water pollutants already exist, including organics, inorganics, and microorganisms. Dyes-contaminated water environments have been generated ever since dyestuffs began to be fabricated and recently, has become one of the largest water defilers in the world. At present, a huge number of the dyestuffs in the industry are daily consumed to color various kinds of materials.[1–3] Crystal violet (CV) and methylene blue (MB), basic dyes, are used a lot for coloring paper, dyeing cotton, and dyeing wools.[2,4,5] Methyl orange (MO), an acidic dye containing the azo group (N=N), is used in the printing, food, pharmaceutical, paper, and textile industries.[2,6] Both basic and acidic dyes have significant concerns because of their toxicity to aquatic creatures and human beings.[6,7] But, the basic dyes are more toxic than the acidic dyes because of their easy interaction with negative cell membrane and/or entrance into living cells, and concentrate in the cytoplasm to cause mitotic poisoning.[4,7]

Adsorption has been shown to be the most effective technique for dye removal because of its easy operation and the ability to treat concentrated dyestuffs with the possibility of regeneration.[1,2,4,7–10] But, most of the developed adsorbents in the literature do not have an effective treatment performance for the effluents that have multiple dyes (basic and acidic), as found in industrial wastewater cases. More recently, regarding increasing types of water pollutions, the exploitation of multifunctional materials has received enormous attention in research communities. To date, there are a few studies on the preparation of multifunctional materials for dye adsorption and microbial purification.[10] For example, Jiang *et al.* (2016) studied the application of a magnetic chitosan–graphene oxide (MCGO) composite as an adsorbent for MO dye (398.08 mg g^{-1}) and antibacterial activity towards *Escherichia coli*.[11] Al-Sagheer *et al.* (2014) investigated the uptake of different dyes (EBT, MV, and MB) and cytotoxicity against different bacteria and fungi using a chitosan-*g*-poly(*N*-acryloylmorpholine) copolymer, and they noted that the copolymer exhibits greater affinities of acid dye adsorption and antibiological activity towards *E. coli*. However, to the best of our survey, there is no literature that explores the antimicrobial and dye adsorption performance of 4,5-diphenyl-

[a]*Analysis and Evaluation Department, Egyptian Petroleum Research Institute, 11727 Nasr City, Cairo, Egypt. E-mail: sherifali@epri.sci.eg; sherifali_r@yahoo.com; Fax: +202 22747433; Tel: +201 228877458*

[b]*Central Laboratories, Egyptian Petroleum Research Institute, 11727 Nasr City, Cairo, Egypt*

[c]*Chemistry Department, Faculty of Science, Ain Shams University, 11566 Abassia, Cairo, Egypt*

2-thioxo-2,5-dihydro-1*H*-pyrrole-3-cabonitrile and protonated carbon nitride (HCN).

In view of the above facts, the aim of this work is to fabricate a new multifunctional material for the effective wastewater remediation from multiple dyes (CV, MB, and MO) pollutants with simultaneous antimicrobial properties. As a result, P3C@CaO–HCN multifunctional nanomaterial prepared by the reaction of 4,5-diphenyl-2-thioxo-2,5-dihydro-1*H*-pyrrole-3-cabonitrile with CaO nanoparticles impregnated onto protonated carbon nitride sheet (HCN) was obtained and characterized. A four-variable three-level Box–Behnken design of experiment (BBD-DOE) was applied to investigate the linear and nonlinear influences of the adsorption variables to provide a mathematic equation for optimization of multi-dyes adsorption. Kinetic, isotherm, and thermodynamic theories were investigated and statistically validated to understand the rate-controlling steps involved in the adsorption application. The antimicrobial activity of the P3C@CaO–HCN nanocomposite was further tested against three selected microorganisms, including *Escherichia coli*, *Pseudomonas aeruginosa*, and *Candida albicans* strains, as widely found pathogens in water environments.

2. Experimental

2.1. Synthesis of 4,5-diphenyl-2-thioxo-2,5-dihydro-1*H*-pyrrole-3-cabonitrile (P3C)

A mixture of 10 mmol 4,5-diphenyl-2-oxo-2,5-dihydro-1*H*-pyrrole-3-cabonitrile[12] and 20 mmol P_2S_5 in 30 mL dry toluene was refluxed for 8 h. After that, the solvent was decanted under reduced pressure and the solid obtained was filtered off, washed, and then recrystallized from benzene to afford dark red needles. The obtained reddish crystals of 4,5-diphenyl-2-thioxo-2,5-dihydro-1*H*-pyrrole-3-cabonitrile (yield 60% and m.p. 476–478 K) was labeled as P3C. The characteristic structure of the obtained P3C (thioxo pyrrole derivative) were presented as follows: FTIR (KBr) cm^{-1}: 3350 (NH), 1250 (CS), 2360 (C≡N). ^{1}H-NMR (DMSO-d_6): δ (ppm) 2.51 (br s, 1H, NH, exchangeable with D_2O), 4.63 (s, 1H, –CHPh), 7.02–7.77 (m, 10H, ArH). MS, *m*/*z* (%): 278 (M^+, 72), 260 (45), 248 (15), 231 (17), 105 (30), 74 (90), 59 (100). Anal. calcd for $C_{17}H_{12}N_2S$ (276.36): C, 73.88; H, 4.38; N, 10.14; S, 11.60. Found: C, 74.01; H, 4.47; N, 9.98; S, 11.82.

2.2. Synthesis of g-C_3N_4 and CaO nanomaterials

The g-C_3N_4 was prepared by microwave thermal condensation of 20 g urea (99%, Aldrich) in a covered alumina crucible for 1 h at 700 watts. The resulting yellow product was then HCl-treated in a quartz reactor containing 1 mol HCl at 348 K under vigorous stirring for 12 h. The protonated product was collected, washed with hot deionized water, and then vacuum dried at 373 K and coded as protonated carbon nitride (HCN).

Calcium oxide nanoparticles were prepared from eggshells. Typically, the free membrane eggshells were grounded and then purified by dichloromethane in an ultrasonic bath for 2 h at 333 K then filtered and dried at 393 K. The powder was then calcined in a microwave oven at 700 watts for 90 minutes and the obtained white powder obtained was coded as CaO nanoparticles (NPs).

2.3. Fabrication of P3C@CaO–HCN nanocomposite adsorbent

The P3C@CaO–HCN nanocomposite was prepared according to the procedure described hereinafter, which is also depicted in Scheme 1. In the first step, a known weight of CaO NPs and HCN (1 : 3) were completely dispersed in 100 mL aqueous ethanolic solution placed in 60 Hz ultrasonic bath for 1 h, then aged overnight at 363 K under stirring. The CaO–HCN nanocomposite obtained was then collected by centrifugation and calcined at 553 K for 2 h. In the next step, the CaO–HCN sample was dispersed in 50 mL ethanol/acetic acid anhydrous (1 : 0.2) mixture solution and sonicated for 30 minutes. To this dispersion, 15 mL ethanol solution of P3C heteroaromatic functional material was added over 3 h. After that, the mixture was aged for another 36 h at 363 K with a stirring speed of 700 rpm. After the reaction stopped, the obtained powder of P3C@CaO–HCN nanocomposite, with nominal ratios of 1 : 3 : 0.5, was collected, washed, and vacuum dried at 363 K.

2.4. Analytical procedures

Melting point was measured on a Gallen Kamp electric melting point apparatus. The ^{1}H-NMR spectra were run at 300 MHz on a GEMINI 300 BB NMR spectrometer using tetramethylsilane (TMS) in DMSO-d_6 as the internal standard. The mass spectra were recorded on a Shimadzu GC-MS QP-1000EX mass spectrometer operating at 70 eV. FTIR spectra were obtained using a KBr disc on a spectrum one Perkin Elmer FT-IR spectrophotometer. The phase structures were determined by X-ray powder diffraction (XRD, Xpert PRO, PAN analytical, Netherlands) at 1.54056 Å Cu Kα radiation and a D8 Bruker diffractometer (40 kV and 30 mA). High-resolution transmission electron microscopy (HR-TEM) images were recorded on a JEOL JEM-2, 100 electron microscope at 200 kV accelerating voltage.

2.5. Batch adsorption tests

Stock water solutions of 2000 μmol L^{-1} of CV, MB, and MO dyes were first prepared in synthetic wastewater containing 1055 mg L^{-1} inorganic dissolved solids similar to the characteristic of previously collected dyestuff industrial wastewater in Egypt (data not shown). All batch adsorption runs were conducted in 125 mL closed shaking flasks at 150 rpm fixed shaking speed.

2.5.1. Box–Behnken design of experiment (BBD-DOE). The optimum variables for optimizing the P3C@CaO–HCN adsorbent for the adsorption of CV, MB, and MO were set by a rotatable, four-variables, three-level Box–Behnken design (BBD). The three-level independent variables were set as solution pH ($X_{pH} = 3, 6, 9$), composite dose ($X_D = 0.5, 1.0, 1.5$ g L^{-1}), initial dye concentrations (X_{Co} = 200, 600, 1000 μmol L^{-1}), and solution temperature (X_T = 288, 308, 328 K). The levels of independent variables were selected based on our assessment of Al-Gharbia textile industries in Egypt (data not shown). The adsorption capacities (q_e, μmol g^{-1}) of CV (Y_{CV}), MB (Y_{MB}) and MO (Y_{MO}) dyes by P3C@CaO–HCN were selected

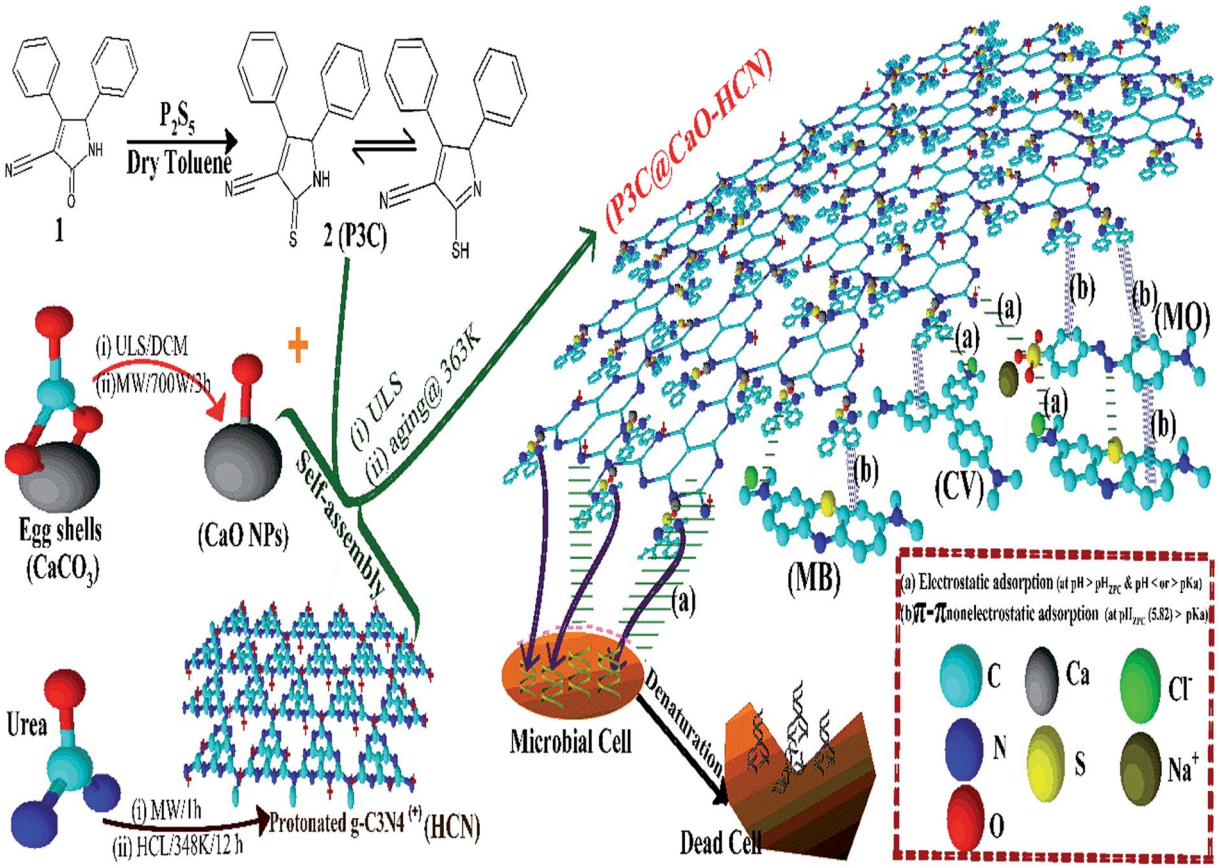

Scheme 1 Diagram of P3C@CaO–HCN nanocomposite preparation procedure and proposed adsorption and antimicrobial mechanisms.

as response factors. Based on the BBD-DOE design matrix, a total of 29 batch experimental runs (runs = $2^4 + 2 \times 4 + 5$ controlled points) were studied. The 29 BBD-DOE response results obtained were then analyzed using the MINITAB (v. 17) and Design-Expert (v. 7.0.1) software programs to develop a numerical regression equation to express the relation between the dyes responses and the independent variables under the tested conditions.

2.5.2. Adsorption studies. For the statistical BBD-DOE adsorption design, 29 series of lab flasks with the desired level of variable combinations were placed on an orbital shaker and agitated for 24 h. At the optimum BBD-DOE conditions: kinetic, thermodynamic, and isotherm studies were conducted. The kinetic and thermodynamic studies were carried out at X_{Co} = 1000 μmol L^{-1} initial dyes concentrations with varying temperatures (288 K to 328 K) for ten intervals of time up to 24 h. The isotherm test was performed using a series of 10 initial dyes concentrations ranging from 50 to 1600 μmol L^{-1}. The other adsorption conditions were set on the basis of the optimum BBD-DOE results obtained. After the adsorption processes, the residual dyes concentrations were determined by a double beam UV-visible spectrophotometer in the supernatant solutions after centrifugation. Dye concentrations in the treated wastewater were calculated from the corresponding linear calibration curves for each dye at their λ_{max} values of 586 nm, 668 nm, and 464 nm for CV, MB, and MO, respectively. The dyes removal percentages (Y%) and adsorption capacities (μmol g^{-1}) were calculated using the following equations (eqn (1) and (2)):

$$Y\% = \frac{(C_0 - C_t)}{C_0} \times 100 \quad (1)$$

$$q_t = \frac{C_0 - C_t}{m} V \quad (2)$$

where C_0 and C_t (μmol L^{-1}) are the dyes concentrations at initial and time t, respectively, V (L) is the water volume, and m (g) is the adsorbent dose.

2.6. Statistical models validation and error analysis

The adequacy of the simulated models and their validation were assessed using different descriptive statics including a non-parametric Mann–Whitney U-test and a parametric two-sample (unpaired) t-test in accordance with the analysis of variance (ANOVA) at a probability level of 0.05.[4] Error statistics, including the root mean square error of prediction (RMSEP), the relative standard error of prediction (RSEP), chi-square (χ^2) tests, and the average relative error (ARE%), were also calculated to reflect the suitability of the simulated mathematical models to predict the adsorption responses.[4,13,14] The statistical validation and error studies were checked using the solver add-in with Microsoft Excel@2013, MINITAB (v. 17), and IBM-SPSS (v. 21)

statistical software packages for the verification of the results obtained.

$$\mathrm{RMSEP} = \sqrt{\frac{\sum_{i=1}^{N}\left(Y_{\mathrm{pred,\,i}} - Y_{\mathrm{exp,\,i}}\right)^2}{N}} \quad (3)$$

$$\mathrm{RSEP} = \sqrt{\frac{\sum_{i=1}^{N}\left(Y_{\mathrm{pred,\,i}} - Y_{\mathrm{exp,\,i}}\right)^2}{\sum_{i=1}^{N}\left(Y_{\mathrm{exp,\,i}}\right)^2}} \times 100 \quad (4)$$

$$\chi^2 = \sum_{i=1}^{N}\left|\frac{\left(Y_{\mathrm{exp},\,i} - Y_{\mathrm{pred},\,i}\right)}{Y_{\mathrm{exp},\,i}}\right|^2 \quad (5)$$

$$\mathrm{ARE}\% = \frac{100}{N}\sum_{i=1}^{N}\left(\frac{\left(Y_{\mathrm{exp},\,i} - Y_{\mathrm{pred},\,i}\right)}{Y_{\mathrm{exp},\,i}}\right) \quad (6)$$

where $Y_{\mathrm{pred},i}$ and $Y_{\mathrm{exp},i}$ are the model predicted and experimental response values, and N is the number of experimental runs.

3. Results and discussion

Pyrrole is an important heterocycle because its structure is incorporated into many natural products *e.g.*, heme, chlorophyll, vitamin B12, and the bile pigment. Also, the pyrrole ring is present in various drugs, including immunosuppressants, analgesics, anti-tubercular agents, and COX-2 inhibitors. In our earlier investigation,[12] 4,5-diphenyl-2-oxo-2,5-dihydro-1*H*-pyrrole-3-cabonitrile preparation was reported by our research group. In the present work, we have modified the pyrrolone derivatives into its thioxo derivative through converting the oxocarbonyl group (C=O) at position-2 into the thiocarbonyl group (C=S) by reaction with P_2S_5 in dry toluene Scheme 1 (*cf.* Experimental part). The thiocarbonyl group, which is known to be more electron rich and polarizable than the C=O group, exists as a thione/thiol tautomer with the N–H group in the 1*H*-pyrrole derivative. The presence of the two active functionalities of thiol (–SH) and cyanide (–CN) obtained in the 4,5-diphenyl-2-thioxo-2,5-dihydro-1*H*-pyrrole-3-cabonitrile (P3C) promoted our interest to construct an active functional component onto CaO–HCN nanocomposite through the thiol group. This results in the formation of a strong S–O bond on the CaO–HCN nanocomposite surface and free cyanide (–C≡N) group, as confirmed by FTIR (*cf.* Section 3.1 part). The developed P3C@CaO–HCN showed multifunctional application for the adsorption of CV, MB, and MO organic dyes and wastewater purification from microbial pathogens because of the free cyanide group, as described hereinafter and depicted in Scheme 1.

3.1. Structure characterization of the P3C@CaO–HCN

XRD spectra were used to test the phase structures and purity of the samples. The set of XRD diffraction peaks (Fig. 1a) show the pure crystal phases of CaO NPs ($2\theta = 18.10°$, 32.3°, 37.4°, 53.90°, 64.20°, and 67.40°) and g-C_3N_4 (HCN) ($2\theta = 13°$ and 27.4°) with no other impurity peaks. For the CaO–HCN hybrid nanocomposite, the XRD patterns assigned to both CaO NPs and g-C_3N_4 were found beside a minor amount of $Ca(OH)_2$ phase that resulted during CaO impregnation in the aqueous phase. The HCN peak at 27.4° (0 0 2) became weaker, which was the result from restraining the stacking of HCN perpendicular to the (0 0 2) directions (the graphitic stacking of the conjugated aromatic system) owing to the introduction of CaO NPs.[15] These results imply that CaO NPs deposited onto the surface of the HCN sheet and did not incorporate into the HCN lattice.[15,16] Also, the XRD data showed that the microwave thermal method used in our study was sufficient to achieve complete thermal decomposition of carbonate in eggshells to pure CaO phase and thermal condensation of urea to graphitic carbon nitride (g-C_3N_4). The determined crystallite size of the prepared CaO/g-C_3N_4 sample using the Scherrer formula[17] at $2\theta = 37.4°$ was computed to be 65.6 nm compared to CaO NPs crystal size of 58.42 nm.

FTIR of the functional P3C@CaO–HCN nanocomposite (Fig. 1b) showed similar characteristic features to their starting components with a slight red shift to a higher wavenumber compared to HCN, CaO NPs, and P3C materials. A band ranging from 3000–3600 cm^{-1} originated from the vibration modes of the free N–H (pyrrole group) and the O–H of adsorbed H_2O by CaO NPs. The sharp breathing vibration band at *ca.* 810 cm^{-1} was assigned to the g-C_3N_4 tri-s-triazine units.[18] Absorption bands in the region between 1200–1700 cm^{-1} corresponded to the skeletal C–N heterocycle stretches, comprising trigonal (N–$(C)_3$) and bridging C–NH–C units of the extended C–N–C network at g-C_3N_4.[18] On the contrary, the decrease of the intensive bands at *ca.* 3600 cm^{-1} (O–H) and *ca.* 500 cm^{-1} (Ca–O vibration) in P3C@CaO–HCN compared to starting components is a sign for P3C complexation onto the CaO NPs surface rather than HCN. The disappearance of the C=S thiocarbonyl stretch band at *ca.* 1250 cm^{-1} (P3C) and the appearance of bands at *ca.*760 cm^{-1} and 1015 cm^{-1} can be ascribed to the S–O stretching bonds (P3C@CaO–HCN) between P3C functionalities and Ca–O through thiol groups. These characteristic results suggest that the strengthening (S–O) interaction bond in the resultant P3C@CaO–HCN nanocomposite was developed between P3C and CaO NPs during functionalization approach.

The P3C@CaO–HCN morphological structure was examined using HRTEM, as shown in Fig. 2a. The HRTEM image showed spherical CaO NPs incorporated with both de-agglomerated and agglomerated distributions on the smooth surface of HCN with an average diameter of 60.7 nm. Also, HCN displayed a platelet-like morphology and a two-dimensional sheet structure. The pH zero point charge (pH_{ZPC}) of HCN, CaO NPs, and P3C@CaO–HCN samples were determined by both potentiometric mass titration and salt addition methods after 24 h of equilibration.[19] The resultant pH values using a pH meter model Seven Go, IP67 (Mettler Toledo) are plotted in Fig. 2b. A significant change in the pH_{ZPC} surface charge properties was observed, which was calculated to be 5.09, 10.52, and 5.82 for HCN, CaO NPs, and P3C@CaO–HCN, respectively.

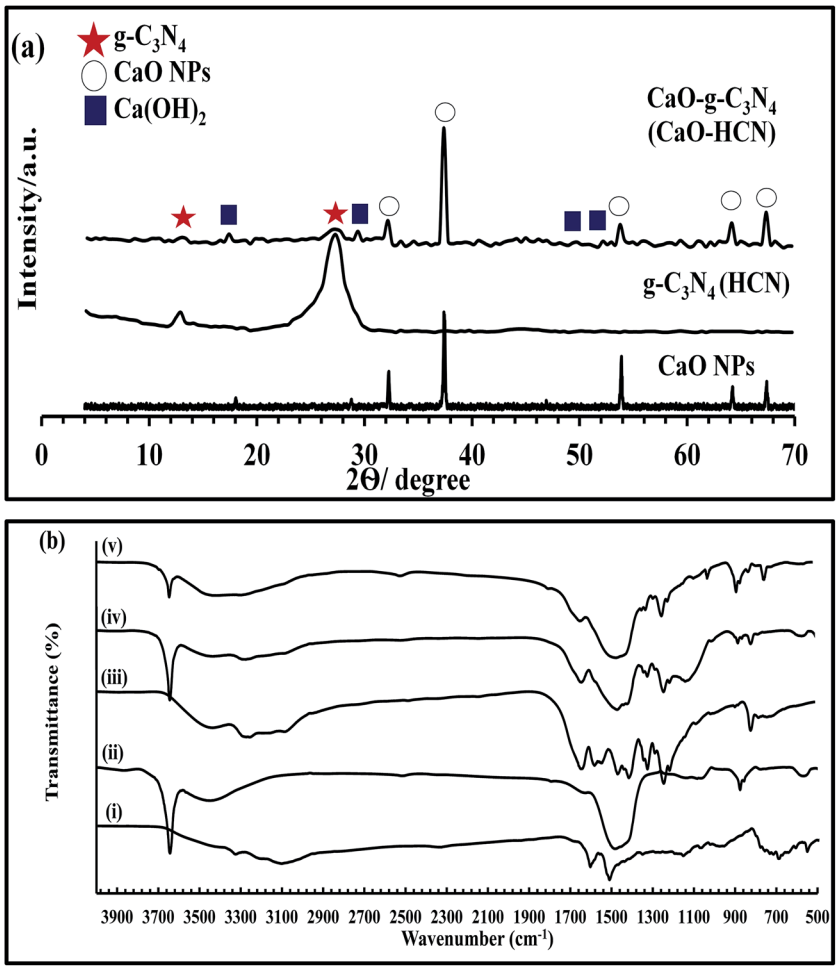

Fig. 1 (a) XRD patterns (CaO NPs, HCN, and CaO–HCN) and (b) FT-IR spectra of (i) P3C, (ii) CaO NPs, (ii) HCN, (iv) CaO–HCN, and (v) P3C@CaO–HCN materials.

3.2. Statistical modeling and optimization of the adsorption variables by RSM method

3.2.1. Statistical model simulation. A three-level BBD-DOE approach was adopted for studying the linear and simultaneous effects of the four adsorption variables to enhance the adsorption properties of P3C@CaO–HCN. Based on the BBD-DOE experiments, the obtained minimum to maximum adsorption capacity responses were found to be ranged respectively between 110.8 to 1013.9 μmol g^{-1}, 116.5 to 1455.8 μmol g^{-1}, and 69.7 to 1007.9 μmol g^{-1} for CV, MB, and MO dyes. The BBD coupled with DOE analysis suggests the nonlinear polynomial regression model (eqn (7)) as the best-fitted expression between the dyes responses and the coded variables (X_{pH}, X_D, X_{Co}, X_T) with β as the regression coefficient term.

$$Y = \beta_0 + \beta_1 X_{pH} + \beta_2 X_D + \beta_3 X_{Co} + \beta_4 X_T + \beta_{12} X_{pH} X_D + \beta_{13} X_{pH} X_{Co} + \beta_{14} X_{pH} X_T + \beta_{23} X_D X_{Co} + \beta_{24} X_D X_T + \beta_{34} X_{Co} X_T + \beta_{11} X_{pH}^2 + \beta_{22} X_D^2 + \beta_{33} X_{Co}^2 + \beta_{44} X_T^2 \quad (7)$$

The quality of the polynomial equation (eqn (7)) was confirmed by the high correlation coefficients (R_{Adj}^2 0.997–0.991 and R_{Pred}^2 0.996–0.989), which were close to unity with high accuracy of approximation ($R^2 = 0.998$). A low significant errors deviation in the conducted design further confirmed the suitability of the developed equation to fit the CV, MB, and MO adsorption responses. The RMSEP of 9.1, 14.04, and 11.83, RSEP of 18.63%, 25.36%, and 32.89%, and calculated χ^2 values of 7.68, 15.29, and 16.07 less than critical χ^2 ($\chi_{\alpha,(n-1)}^2$ 41.34) were calculated for CV, MB, and MO adsorption responses, respectively. The statistic low coefficient of variation (C.V. of 2.92–3.72%) and adequate precision ratio of 82.65–97.99 greater than 4,[4] reveal an adequate signal for the polynomial equation (eqn (7)) to predict the dyes responses data. Moreover, the ANOVA results listed in Table 1 indicated that the polynomial equation was significant. This is evident from the Student's *t*-test (t_{model} = 56.76–75.81 ≫ t_{crit} 2.049) and Fisher's *F*-test (F_{model} = 447.33–626.28 ≫ $F_{crit} = F_{0.05,df,(n-df+1)} = 2.484$) with a very low probability value ($p_{model} < 0.0001$). Thus, the simulated model can be efficiently used in the optimization and predication of dyes adsorption responses by the fabricated nanocomposite adsorbent in the design constrain level.

3.2.2. Effects of model components on dye adsorption efficiencies. The influence of the model components and their coefficient terms (β) on the studied dyes adsorption were

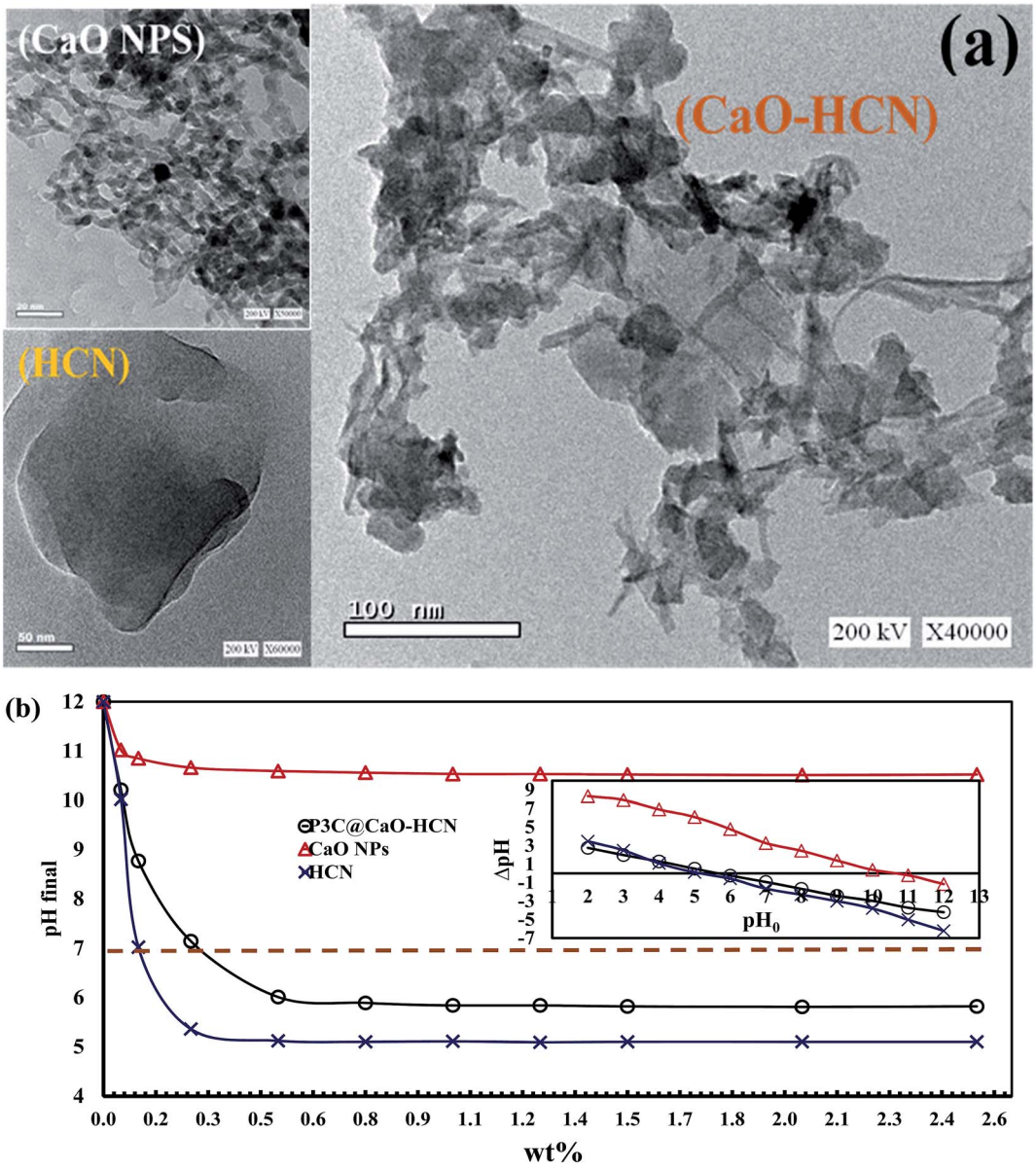

Fig. 2 (a) TEM images and (b) pH_{ZPC} curves of CaO NPs, HCN and P3C@CaO–HCN nanocomposite materials.

further tested by the ANOVA tools listed in Table 1. Statistical F_{Calc}, t_{Calc}, and p-tools indicated that the linear model components showed high significant effects on the dyes responses than their respective interactive and quadratic effects (Table 1). The results were reflected also by the estimated β values and the percent contribution (PC%) tabulated in Table 2. As seen, the linear components represented the highest influence level with a total PC% of 90.1%, 86.2%, and 85.2%; but, the quadratic components showed the lowest contribution with a total PC% of 4.2%, 4.6% and 4.8% for the CV, MB, and MO dyes adsorption, respectively. In general, the influential level of linear components can be arranged as initial dye concentrations (X_{Co} = 44.8%, 46.2%, and 42.6%) > composite dose (X_D = 35.4%, 36.97%, and 29.5%) > solution pH (X_{pH} = 8.2%, 2.7%, and 12.6%) > temperature (X_T = 1.7%, 0.36%, and 0.47%) on the dyes adsorption responses. Among the equation components, the interaction term of $X_D X_T$ (PC% = 0.001–0.05%; p = 0.071–0.541) and quadratic temperature term (X_T^2, PC% = 0.001–0.02%; p = 0.236–0.984) showed the lowest influential effect on the dyes adsorption. As a fact, the coefficient sign determines the effect direction on the studied responses.[4,13,20] The estimated coefficient values (Table 2) showed that the X_D exhibited an unfavorable or antagonistic effect (negative sign) on the dyes responses in addition to the pH variable (X_{pH}) on MO adsorption response only. But the other linear variables showed positive coefficient terms (synergistic effect) on dyes adsorption responses.

3.2.3. BBD-DOE optimization of adsorption process. The 3D response surface contour plots were more helpful in facilitating the straightforward investigation of the experimental variables on the dyes responses.[4,20] Based on the simulated polynomial equation (eqn (7)), the 3D contour plots for the CV,

Table 1 ANOVA[a] results of the CV, MB, and MO responses by P3C@CaO–HCN nanocomposite adsorbent

		SS			*F*-Value			Prob > *F*		
Source	df	CV	MB	MO	CV	MB	MO	CV	MB	MO
Model	14	1 504 132.8	2 553 355.5	1 912 533.8	626.3	532.5	467.0	<0.0001	<0.0001	<0.0001
X_{pH}	1	123 848.6	68 927.1	242 111.8	721.9	201.3	827.7	<0.0001	<0.0001	<0.0001
X_D	1	533 950.1	945 749.9	565 372.2	3112.5	2761.5	1932.8	<0.0001	<0.0001	<0.0001
X_{Co}	1	674 328.3	1 180 919.0	816 988.7	3930.8	3448.1	2793.1	<0.0001	<0.0001	<0.0001
X_T	1	25 167.8	9150.5	8954.0	146.7	26.7	30.6	<0.0001	0.0001	<0.0001
$X_{pH}X_D$	1	6048.7	9096.6	45 405.4	35.3	26.6	155.2	<0.0001	0.0001	<0.0001
$X_{pH}X_{Co}$	1	18 413.6	9108.9	37 073.9	107.3	26.6	126.7	<0.0001	0.0001	<0.0001
$X_{pH}X_T$	1	4175.6	1253.0	221.5	24.3	3.7	0.8	0.0002	0.0765	0.3741
X_DX_{Co}	1	28 218.4	97 195.0	4961.1	164.5	283.8	17.0	<0.0001	<0.0001	0.0007
X_DX_T	1	67.3	522.5	999.7	0.4	1.5	3.4	0.5413	0.2371	0.0714
$X_{Co}X_T$	1	6300.1	892.8	3100.0	36.7	2.6	10.6	<0.0001	0.1287	0.0040
X_{pH}^2	1	7428.3	46 226.8	62 815.4	43.3	135.0	213.0	<0.0001	<0.0001	<0.0001
X_D^2	1	48 461.4	142 760.8	62 708.5	282.5	416.8	216.1	<0.0001	<0.0001	<0.0001
X_{Co}^2	1	11 976.8	75.5	30 338.0	69.8	0.2	102.5	<0.0001	0.6459	<0.0001
X_T^2	1	0.1	526.1	69.4	0.04	1.5	0.2	0.9841	0.2356	0.6154
Residual	14	2401.7	4794.7	3679.3						
Lack of fit	10	2281.9	4493.7	3449.2	7.6	6.0	2.1	0.0326	0.0499	0.0496
Pure error	4	119.8	301.0	230.2						
Cor total	28	1 506 534.5	2 558 150.2	1 916 213.2						

[a] ANOVA: analysis of variance determined by Design-Expert (v. 7.0.1) software.

Table 2 Multiple regression[a] and BBD-DOE coefficients results

		Effect			Estimated coefficient			*t*-Value			PC[b] (%)		
Model components	Model terms	CV	MB	MO	CV	MB	MO	CV	MB	MO	CV	MB	MO
Intercept	β_0	—	—	—	444.1	519.4	522.1	75.81	62.76	72.01	—	—	—
X_{pH}	β_1	203.18	151.58	−284.08	101.6	75.8	−142.0	26.87	14.19	−30.35	8.22	2.69	12.63
X_D	β_2	−421.88	−561.47	−434.12	−210.9	−280.7	−217.1	−55.79	−52.55	−46.38	35.44	36.97	29.50
X_{Co}	β_3	474.11	627.41	521.85	237.1	313.7	260.9	62.7	58.72	55.76	44.76	46.16	42.64
X_T	β_4	91.59	55.23	54.63	45.8	27.6	27.3	12.11	5.17	5.84	1.67	0.36	0.47
$X_{pH}X_D$	β_{12}	−77.77	−95.38	213.09	−38.9	−47.7	106.5	−5.94	−5.15	13.14	0.40	0.36	2.37
$X_{pH}X_{Co}$	β_{13}	135.7	95.44	−192.55	67.8	47.7	−96.3	10.36	5.16	−11.88	1.22	0.36	1.93
$X_{pH}X_T$	β_{14}	64.62	35.4	−14.88	32.3	17.7	−7.4	4.93	1.91	−0.92	0.28	0.05	0.01
X_DX_{Co}	β_{23}	−167.98	−311.76	−70.44	−84.0	−155.9	−35.2	−12.83	−16.85	−4.34	1.87	3.80	0.26
X_DX_T	β_{24}	−8.2	−22.86	−31.62	−4.1	−11.4	−15.8	−0.63	−1.24	−1.95	0.001	0.02	0.05
$X_{Co}X_T$	β_{34}	79.37	29.88	55.68	39.7	14.9	27.8	6.06	1.61	3.43	0.42	0.03	0.16
X_{pH}^2	β_{11}	−67.68	−168.84	−196.82	−33.8	−84.4	−98.4	−6.58	−11.62	−15.46	0.74	2.98	3.82
X_D^2	β_{22}	172.87	296.71	196.65	86.4	148.4	98.3	16.81	20.42	15.45	3.99	6.01	4.34
X_{Co}^2	β_{33}	−85.94	6.82	−136.78	−43.0	3.4	−68.4	−8.36	0.47	−10.74	0.82	0.01	1.61
X_T^2	β_{44}	−0.21	−18.01	−6.54	−0.1	−9.0	−3.3	−0.02	−1.24	−0.51	0.001	0.02	0.001

[a] Multiple regression analysis calculated by MINITAB (v. 17) software. [b] The percent contribution (PC%) = SS/$\sum$SS × 100.

MB, and MO responses (q_e, μmol g^{-1}) are visualized in Fig. 3. The 3D plots of the $X_{pH}X_D$ interactive term (Fig. 3a) showed that the P3C@CaO–HCN dose (X_D) exhibits an inverse influential effect on adsorption capacity, whereas the effect of solution pH is dependent on the adsorbed dye type. The q_e (μmol g^{-1}) of the basic CV and MB dyes increase with an increase in the entire pH range up to pH 7.5. While the acidic MO dye adsorption capacity is higher at the median pH level of ≈6 and decreased at both very low and high pH levels. The pH-adsorption dependence suggested that the P3C@CaO–HCN adsorption mechanism is a complex interplay between electrostatic and non-electrostatic forces based on solution pH, pH_{ZPC} of the adsorbent, and pK_a of dye molecules (Scheme 1 & adsorption mechanism hereinafter). Because of the solution pH can influence the degree of adsorbent surface charge through protonation or deprotonation of functional active sites on the adsorbent surface and ionization of organic dyes pollutants, the adsorption of dyes molecules is affected by the pH of the water environments.

The interactive effect of $X_{Co}X_D$ on dyes adsorption (Fig. 3b) showed that the X_{Co} has a synergetic effect on the q_e (μmol g^{-1}) responses with decreasing X_D level.[4,20] This trend is explained by assuming that the saturation of all the binding sites on the P3C@CaO–HCN surface is attained at the low X_D level of 0.5 g L^{-1}. However, with an increased X_D level, a higher number

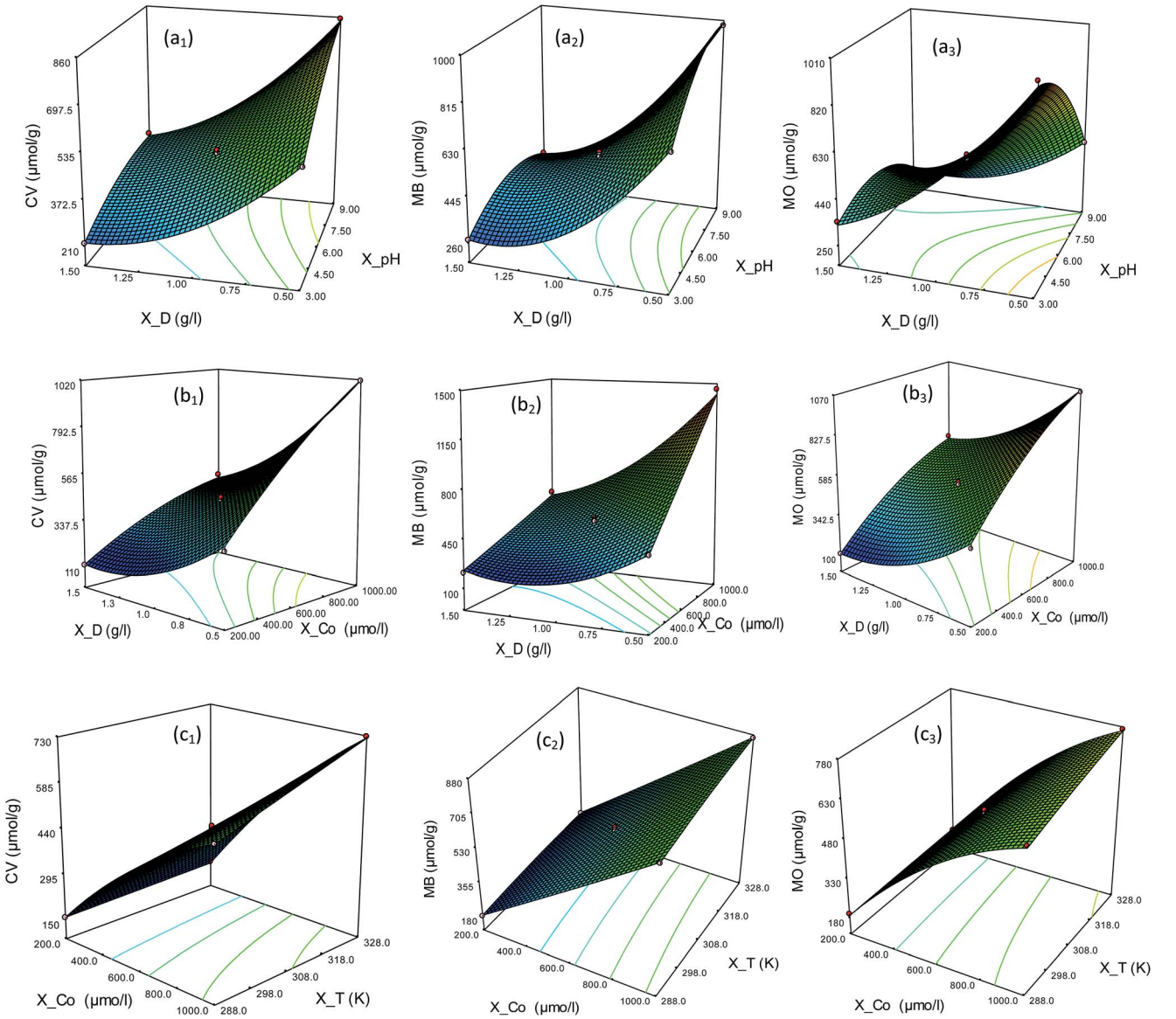

Fig. 3 3D response surface contour plots of CV, MB, and MO dyes adsorption capacities *versus* interaction of: (a) pH and adsorbent dose ($X_{pH}X_D$), (b) initial dyes concentrations and adsorbent dose ($X_{Co}X_D$), and (c) initial dyes concentrations and temperature ($X_{Co}X_T$).

of binding sites would be generated, which decrease the q_e (μmol g^{-1}) responses due to a vacant surface sites that are still unoccupied (equilibrium state not reached). The combined effect of $X_{Co}X_T$ (Fig. 3c) showed that the temperature variable has a low synergetic influence on the dyes responses with parallel contour lines and no interaction with X_{Co}. This finding suggests that the experimental temperature levels possess lower significant influence on dye responses (q_e, μmol g^{-1}), which was confirmed by the lowest linear temperature effect ratio of 91.59, 55.23, and 54.63 for CV, MB, and MO adsorption, respectively in comparable to other linear variables effect levels (Table 2).

In general, the results above revealed that the prepared P3C@CaO–HCN adsorbent has higher dyes adsorption capacities, which was evident from an increase of q_e to 869.18, 1215.1, and 905.8 μmol g^{-1} for CV, MB, and MO, respectively, at an adsorbent dose <0.75 g L^{-1} and increase X_{Co} up to 900 μmol L^{-1}. Consequently, the maximum operating conditions for the applied application were set by solving the developed polynomial regression model (eqn (7)), on the basis of BBD-DOE, and the input variable levels with their linear, quadratic, and interaction terms obtained. The predicted optimal variables levels at X_{Co} = 1000 μmol L^{-1} were then computed as pH = 5.9, P3C@CaO–HN sorbent = 0.5 g L^{-1}, and solution temperature = 307 K with desirability level of 0.96. At those optimum conditions, the maximum CV, MB, and MO predicted q_e (μmol g^{-1}) were 1013.9, 1418, and 1062.1, which are close to the experimental q_e (μmol g^{-1}) of 1018.2, 1429.5, and 1053.8, respectively.

3.3. Adsorption kinetics and thermodynamics

The effect of adsorption contact times on the dyes adsorption performance of P3C@CaO–HCN at temperature ranges from 288 K to 328 K are shown in Fig. 4. As seen, the dyes adsorption

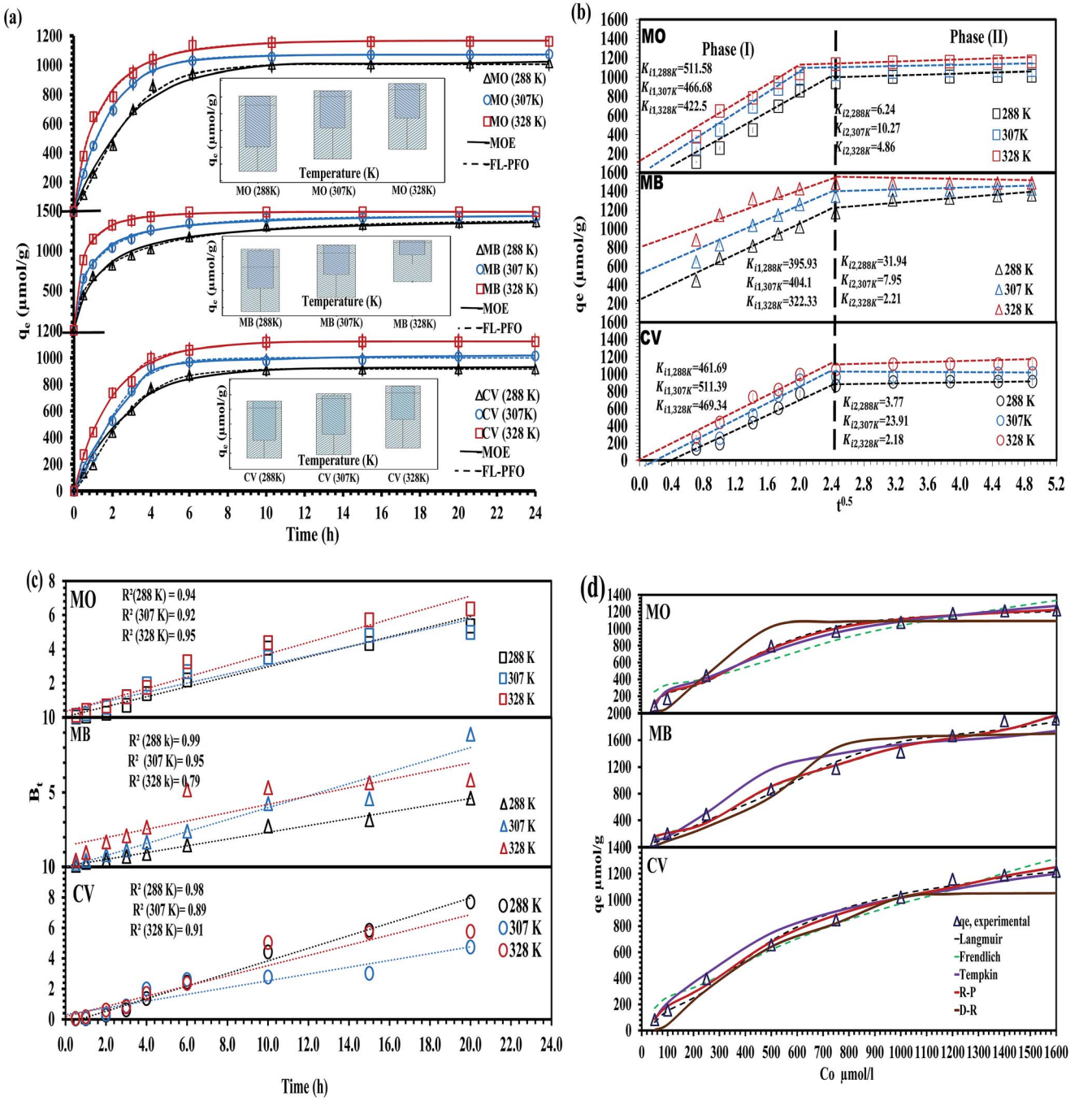

Fig. 4 (a) Effect of contact time on P3C@CaO–HCN adsorption capacities; (b) intra-particle diffusion model; (c) Boyd surface diffusion model; and (d) isotherm models of CV, MB, and MO adsorptions.

appear rapidly rising during the first 4 h followed by a gradual decrease in rate until equilibrium flattening start at 6 h. Temperature also showed a low synergetic influence in the adsorbed amount ($q_{e,exp}$, Fig. 4a) with calculated t_{calc} values of 15.62–8.01, 7.18–5.38, and 8.21–5.62 and p-value range from 0.034 to 0.043 for CV, MB, and MO, respectively. Such results confirmed the above statistical ANOVA results. To determine the adsorption mechanism, five kinetic models, including the pseudo-first-order model (PFOM), pseudo-second-order model (PSOM), Elovich, fractal-like pseudo-first-order (FL-PFOM), and mixed first and second-order (MOE) kinetic models,[21–24] were applied to simulate the dyes adsorption curvatures. Kinetic results and their corresponding mathematical model formula are listed in Table 3. According to the coefficients (R^2) and the resemblance between $q_{e,theo}$ and $q_{e,exp}$ values in Table 3, the dyes adsorption data can be interpreted by FL-PFOM and MOE kinetic expressions. A good mathematical fit does not depend only on the R^2, but it should also be accurate in predicting the experimental data. The good fitness to the FL-PFO and MOE mathematical models (Fig. 4a) imply that the overall rate of dyes

Table 3 Kinetic constants for the adsorption of CV, MB, and MO by P3C@CaO–HCN at different temperatures (288 K, 307 K, and 328 K)

Kinetic parameters		CV			MB			MO			Kinetic equations
		288 K	307 K	328 K	288 K	307 K	328 K	288 K	307 K	328 K	
Experimental q_e (μmol g^{-1})		915.40	1014.00	1120.32	1360.07	1421.99	1487.54	1014.01	1073.90	1161.79	$q_t = q_0(1 - \exp(-K_1 t))$
PFOM	q_0 (μmol g^{-1})	933.72	1017.57	1118.02	1298.28	1368.71	1452.65	1024.15	1070.77	1145.34	
	K_1 (h^{-1})	0.35	0.42	0.51	0.52	0.87	1.66	0.35	0.55	0.68	
	R^2	0.98	0.97	0.99	0.91	0.91	0.94	0.98	0.99	0.97	
FL-PFO	q_0 (μmol g^{-1})	916.1	1009.69	1121.61	1365.52	1436.59	1486.35	1010.34	1068.95	1166.77	$q_t = q_0(1 - \exp(-K_1 t^{\alpha}))$
	K_1 (h^{-1})	0.26	0.32	0.52	0.61	0.87	1.41	0.28	0.54	0.72	
	A	1.34	1.37	0.96	0.59	0.59	0.62	1.27	1.04	0.79	
	R^2	0.996	0.99	0.995	0.993	0.996	0.997	0.992	0.998	0.991	
PSOM	q_0 (μmol g^{-1})	1080.16	1157.38	1243.37	1409.54	1470.08	1512.28	1186.13	1187.42	1249.21	$q_t = K_2 {q_0}^2 t/1 + K_2 q_0 t$
	K_2 (g μmol^{-1} h^{-1})	0.0004	0.0004	0.0005	0.001	0.001	0.002	0.0003	0.0006	0.001	
	$t^{1/2}$ (h)	2.46	1.96	1.46	0.70	0.68	0.33	2.48	1.34	1.00	
	R^2	0.94	0.93	0.97	0.98	0.98	0.99	0.95	0.96	0.98	
Elovich	β (μmol g^{-1} h^{-1})	226.39	232.11	225.72	242.61	204.65	137.59	250.01	211.05	196.67	$q_t = \beta \ln(\propto \beta t)$
	$\propto$ (g μmol^{-1} h^{-2})	0.02	0.02	0.05	0.07	0.35	29.77	0.02	0.06	0.14	
	R^2	0.90	0.86	0.90	0.94	0.92	0.80	0.92	0.87	0.88	
MOE	q_0 (μmol g^{-1})	913.94	1016.59	1121.24	1389.87	1433.29	1488.42	1021.18	1071.78	1167.17	$q_t = q_0 \frac{1 - \exp(-K_1 t)}{1 - F \exp(-K_1 t)}$
	K_1 (h^{-1})	0.35	0.42	0.45	0.01	0.03	0.36	0.35	0.55	0.33	
	F	0.001	0.001	0.154	1.000	0.975	0.866	0.001	0.001	0.640	
	R^2	0.981	0.973	0.995	0.982	0.988	0.998	0.982	0.998	0.990	

adsorption is time dependent on heterogeneous sites on the P3C@CaO–HCN surface and the adsorption behavior changes with the lapse of time.[22,24]

The surface diffusion and intra-particle diffusion models, such as the Boyd model and Weber and Morris model (WMM), were further studied to determine the diffusion mechanism.[23,25] Application of the WMM model (Fig. 4b) showed two-linear adsorption stages. In the initial macro-pore diffusion phase I (${R_1}^2$ 0.902–0.991), most obtainable P3C@CaO–HCN adsorbing sites were utilized by 80–90% of the adsorbed dyes within 2.45 $h^{0.5} \approx 6$ h. The second micro-pore diffusion phase II (${R_2}^2$ 0.857–0.983) is attributed to a slow diffusion, generated with the lapse of time. As seen in Fig. 4b, the WMM empirical relationship states that the intra-particle diffusion is not the rate-factor because the two phase (I and II) lines do not pass through the origin. The diffusion rate constants, K_i (μmol g^{-1} $h^{0.5}$), were found to exhibit a low significant dependence on the studied temperature ranges. Additionally, the Boyd model showed that the calculated B_t points, the time coordinate of Boyd's expression, were scattered around the linear lines with good correlation values R^2 of 0.85–0.97 for dyes adsorption (Fig. 4c). But, the linear lines of Boyd's curves (Fig. 4c) for the adsorbed dyes passes through the origin, which ascertained that the adsorption rates on P3C@CaO–HCN are governed by an initial boundary layer resistance and film diffusion mechanism.

The low significant effect of temperature levels (288 to 328 K) was further confirmed by the calculated thermodynamic constants using the Van't Hoff formula[21,26,27] at $C_0 = 1000$ μmol L^{-1}. The calculated positive enthalpy changes ($\Delta H^\circ = 8.58$, 6.43, and 6.17 kJ mol^{-1}) and entropy changes ($\Delta S^\circ = 0.034$, 0.034, and 0.027 kJ mol^{-1}) for CV, MB, and MO adsorbed dyes indicate an endothermic adsorption, which is consistent with the kinetics and BBD-DOE results. The low magnitude of the calculated ΔH°, less than 20.9 kJ mol^{-1}, reveal that the adsorption is non-electrostatic physical adsorption at optimum conditions.[21,26] In addition, the determined Gibb's free energy changes (ΔG°) for CV, MB, and MO dyes are $\leftarrow$1.26 to $\leftarrow$2.62 kJ mol^{-1}, $\leftarrow$3.46 to $\leftarrow$4.49 kJ mol^{-1}, and $\leftarrow$1.70 to $\leftarrow$2.51 kJ mol^{-1} at 288 K to 328 K, respectively. The negative values of ΔG° suggests spontaneity and feasibility of favorable adsorption by P3C@CaO–HCN. This kind of low significant temperature dependence of the adsorbed dyes by P3C@CaO–HCN adsorbent reflects the film diffusion mechanism of dyes into the adsorbent.

3.4. Equilibrium isotherm studies

The isotherm provides information on dyes adsorption and the commercial viability of the P3C@CaO–HCN nanocomposite material for adsorption applications. A nonlinear regression solving of the Langmuir, Temkin, Freundlich, Redlich–Peterson (R–P), and Dubinin–Radushkevich (D–R) isotherm models[21,26,27] were applied to simulate the equilibrium dyes adsorption results. The simulated nonlinear isotherm expressions for the adsorbed dyes by P3C@CaO–HCN and their coefficient R^2 values are tabulated in Table 4. According to the determined coefficient R^2 value, the R–P isotherm ($R^2 > 0.99$) showed the best-fitting of the dyes adsorption data and the poorest-fitting was found for the D–R model ($R^2 = 0.92$–0.87). The R–P isotherm is a mix of Langmuir–Freundlich equations, and the R–P exponent

Table 4 Isothermal equations and determination coefficients of CV, MB, and MO dyes adsorption onto P3C@CaO–HCN nanocomposite adsorbent

	Simulated mathematical isotherm equations			R^2		
Isotherm models	CV	MB	MO	CV	MB	MO
Langmuir	$q_e = 1449.40\frac{0.005C_e}{1+0.005C_e}$ $R_L = 0.154$	$q_e = 2221.56\frac{0.008C_e}{1+0.008C_e}$ $R_L = 0.11$	$q_e = 1284.37\frac{0.015C_e}{1+0.015C_e}$ $R_L = 0.06$	0.99	0.95	0.99
Freundlich	$q_e = 67.192{C_e}^{1/2.32}$	$q_e = 203.26{C_e}^{1/2.84}$	$q_e = 137.33{C_e}^{1/3.03}$	0.97	0.99	0.94
Temkin	$q_e = 259.14\ \ln(0.103C_e)$	$q_e = 253.69\ \ln(0.147C_e)$	$q_e = 239.02\ \ln(0.2C_e)$	0.98	0.94	0.98
Redlich–Peterson (R–P)	$q_e = \frac{11.399C_e}{1+0.027{C_e}^{0.86}}$	$q_e = \frac{1395.09C_e}{1+6.38{C_e}^{0.59}}$	$q_e = \frac{21.28C_e}{1+0.02{C_e}^{0.95}}$	0.99	0.99	0.99
Dubinin–Radushkevich (D–R)	$q_e = 1053.88\ \exp(-0.001\varepsilon^2)$	$q_e = 1713.38\ \exp(-0.0006\varepsilon^2)$	$q_e = 1092.61\ \exp(-0.0001\varepsilon^2)$	0.87	0.87	0.92

constant ($0 < b < 1$) can characterize the adsorption isotherm favorability.[26] Tabulated isotherm expressions (Table 4) and their graphical representations (Fig. 4d) showed that the Langmuir model is the preferable isotherm ($R^2 = 0.99$) for CV and MO adsorption (b = 0.86 and 0.95, respectively); whereas MB adsorption obeys the Freundlich isotherm (R^2 = 0.99 and b = 0.59). The dimensionless separation factor, R_L, of 0.06–0.15 at C_0 = 1000 μmol L^{-1}, and Freundlich n exponent factor (n = 2.32–3.03) further confirmed the favorable adsorption isotherm by P3C@CaO–HCN. Isotherm results indicate that the P3C@CaO–HCN surfaces have a certain degree of heterogeneous binding sites, as further revealed by the Temkin model (B_T = 239.02–259.14 J mol^{-1} and R^2 = 0.94–0.98).[26,27] Fig. 4d also shows that the adsorption capacities of dyes sharply increase to reach a plateau of maximum equilibrium at initial concentrations of 1200 μmol L^{-1} CV, 1450 μmol L^{-1} MB, and 1100 μmol L^{-1} MO dye. At these concentration points, the maximum experimental q_e (μmol g^{-1}) were recorded as 1227.8, 1915.8, and 1221 μmol g^{-1} for CV, MB, and MO dyes, respectively.

3.5. Adsorption mechanism

Regarding the resultant data above, it can be suggested that the high performance of the P3C@Cao–HCN adsorbent towards both basic and acidic dyes (CV, MB, and MO) may be ascribed to complex adsorption interactions. In addition, the adsorption interactions showed a low B_T and ΔH° binding energy with heterogeneous binding sites including electrostatic and non-electrostatic mechanisms, and the rate-controlling step is pH-dependent.

Herein, the potential mechanism involved was expected to be related to the electrostatic interaction as the predominant force at high and low pH levels. With increased pH > pH_{ZPC} (5.82), CV and MB basic dyes adsorption were enhanced due to electrostatic forces developed between acidic surface sites of P3C@Cao–HCN adsorbent and positive charge densities of CV and MB cations, which is unfavorable for the adsorption of MO acidic dye due to the electrostatic repulsion.[4,28–30] In this case, it can be said that the adsorption of cationic dyes is fine and can more easily take place when using alkaline pH. At highly acidic conditions (pH < 4), the adsorption capacities of both basic (CV and MB) and acidic (MO) dyes decreased, because of the higher protonation H^+ levels. The high concentrations of positive H^+ ions associate to the P3C@CaO–HCN surface and form positively protonated surface sites. The developed protonated surface generates electrostatic repulsion with basic CV and MB cations and hydronium counter ions around acidic MO anions (SO_3^-) in the bulk water solution, leading to decrease their adsorption capacities. A similar observation was recorded at highly alkaline pH (pH > 8) because of a relatively higher number of HO^- groups in solution. In fact, such an electrostatic interaction mechanism is possible between the electron pairs of the N–H group in the 1*H*-pyrrole derivative of the P3C functionalities or tri-s-triazine units (bridging C–NH–C units) of HCN. Otherwise, at near neutral pH ≈ 6, approximately equal pH_{ZPC} (5.82) > pK_a of CV (pK_a = 5.31), MB (pK_a = 3.8), and MO (pK_a = 3.47), the main predominant mechanism could be controlled by non-electrostatic attraction forces. Such non-electrostatic interactions could include π–π stacking interaction and hydrophobic–hydrophobic mechanism, which could be more favored for the MO anionic dye than basic one. The π–π adsorption mechanism can be developed between the π-orbitals in the aromatic ring of dyes molecules and delocalized π-electrons of the C=C double bonds of HCN nanosheets or aromatic binding sites on the P3C functional surface of adsorbent. P3C@CaO–HCN adsorbent can also interact with dyes molecules *via* a hydrophobic–hydrophobic mechanism between the di-phenyl groups in the pyrrolone derivatives of P3C functionality at positions 4 and 5 of 1*H*-pyrrole derivative and aromatic rings of dyes molecules. This is worthwhile to point out because the P3C@Cao–HCN is an effective adsorbent in the adsorption of both cationic and anionic organic dyes with counter charges.

3.6. Models validation and error analysis

Statistical error parameters for the best-fitted models were computed in this work to confirm the suitability of the overall simulated kinetics (FL-PFO and MOE) and isotherm (Langmuir, Freundlich, and R–P) mathematical expressions to the experimental results. First, a non-parametric Mann–Whitney *U*-test, a parametric (unpaired) *t*-test, and a one-way ANOVA were conducted to test significance difference between the experimental (Y_{exp}) and the predicted (Y_{pred}) dyes adsorption capacities.[4] The calculated Mann–Whitney *z*-score of 0.75–0.04, less

than unity, associated with the two-tailed p-value of 0.59–0.987 greater than the chosen level of $p = 0.05$ (95% confidence) imply the suitability of the above selected fitted expressions. Also, the calculated statistic tools from one-way ANOVA were found to be in the range of $t_{cal} = 0.001$–0.39 and $F_{cal} = 0.0001$–0.31, which are lower than the critical values of $t_{crit} = \pm 2.41$, and $F_{crit} = 3.73$. Second, the experimental and predicted output response variables (q_e, μmol g^{-1}) for each set of validation points were used to compute the chi-square (χ^2), RSEP, RMSEP, and %ARE error values. Notably, low error results were recorded using RMSEP (2.08–2.81), RSEP (1.12–2.13), %ARE (2.17–4.65%), and χ^2 (0.13–0.15 $\ll$ critical $\chi_{\alpha,(df=n-1)}{}^2$ of 16.92) with a high correlation ($R^2 =$ 0.992 to 0.999) between Y_{exp} and Y_{pred}. In this case, at 95% certainty, the experimental dyes adsorption results by P3C@CaoO–HCN were well described by the fitted mathematical expressions above as confirmed by the calculated statistics with the lowest errors difference between the two set of output responses (Y_{pred} and Y_{exp}).[4]

3.7. Antimicrobial activity

The synthesized P3C@CaO–HCN nanocomposite was further screened for its *in vitro* antimicrobial activity against three free-living pathogenic strains of *Escherichia coli*(bacteria), *Pseudomonas aeruginosa* (bacteria), and *Candida albicans* (yeast). Luria-Bertani (LB) broth containing different concentrations of P3C@CaO–HCN (C_0 = 100, 250, 500, 1000, and 2500 mg L^{-1}) and 10^5 CFU mL^{-1} initial pathogenic cell was used to test the antimicrobial activity at 310 K and 150 rpm shaking speed. An inhibitory percentage rate (I%, eqn (9)) at the mid-exponential microbial growth was measured against microbial culture blanks as a positive control.

$$I\% = \frac{(CFU_{PC} - CFU_{ACo})}{CFU_{PC}} \times 100 \quad (9)$$

where, CFU_{PC} and CFU_{ACo} are the total strains colony forming unit (CFU mL^{-1}) in the absence and presence of the composite, respectively. The inhibitory rate (I%) of P3C@CaO–HCN against *E. coli*, *P. aeruginosa*, and *C. albicans* pathogens is shown in Fig. 5. It is seen that the cytotoxicity effect toward the three pathogens was increased with the increasing concentration of P3C@CaO–HCN. The visualized reduction of cell viability was escalated with *E. coli* compared to *P. aeruginosa* and *C. albicans* at given concentrations, which implied that the antimicrobial activity of P3C@CaO–HCN was not only P3C@CaO–HCN dependent but also microbial dependent. As shown in Fig. 5, the P3C@CaO–HCN loaded cultures also exhibited a high significant antimicrobial activity with higher reduction percentage on *E. coli* (93.5%) and *C. albicans* (85.8%) compared to a moderate I% against *P. aeruginosa* (61.54%) at C_0 of 2500 mg L^{-1} P3C@CaO–HCN. Also, the P3C@CaO–HCN showed a minimum inhibitory concentration (MIC) at 500 mg L^{-1} with I% of 87.9%, 46.9%, and 72.5% for *E. coli*, *P. aeruginosa*, and *C. albicans*, respectively. Losing microbial viability may result from the free cyanide (C≡N) group on 4,5-diphenyl-2-thioxo-2,5-dihydro-1*H*-pyrrole-3-cabonitrile functionality and the protonated g-C_3N_4 (HCN) nanosheet. In this case, the nanocomposite provides electrostatic adsorption of a negatively charged microbial surface onto the positive HCN nanosheet, and subsequently, the free C≡N functionalities tightly bound to ubiquinone whole cells (Scheme 1). This may lead to induced microbial membrane stress, and hence, disrupt their metabolic system leading to cell death.[10,11]

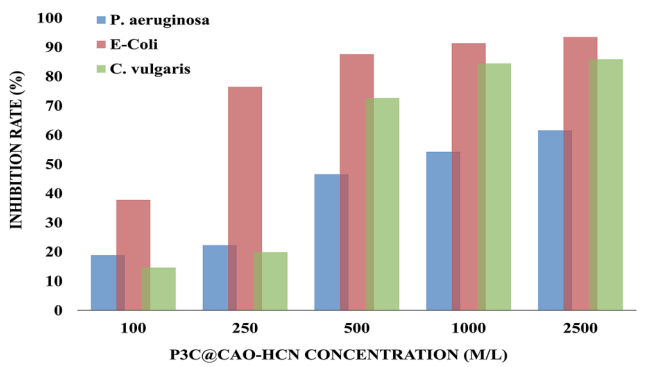

Fig. 5 Antimicrobial activity of P3C@CaO–HCN against *E. coli*, *P. aeruginosa*, and *C. albicans* microbial pathogens.

4. Conclusions

In this work, P3C@CaO–HCN nanocomposite, a new multifunctional nanomaterial, was fabricated for wastewater remediation from organic dye and microbial contaminants. The P3C@CaO–HCN was prepared by the reaction of 4,5-diphenyl-2-thioxo-2,5-dihydro-1*H*-pyrrole-3-cabonitrile with CaO nanoparticles impregnated onto protonated carbon nitride (HCN). Adsorption experiments with CV, MB, and MO organic dyes using the Box–Behnken design outlined that the adsorption mechanism of P3C@CaO–HCN depends on the molecular dye structure and the charge densities of the adsorbent surface, which varies with solution pH levels. The adsorption data was fitted well with both the fractal-like pseudo-first-order (FL-PFOM), and mixed first and second-orders (MOE) kinetic models and Redlich–Peterson (R–P) isotherm model. The validation data confirmed the high suitability of the selected models to simulate the experimental adsorption results ($R^2 >$ 0.99, RMSEP ≤ 2.81, RSEP ≤ 2.13, % ARE ≤ 4.65%, and $\chi^2 \leq$ 0.15 less than critical $\chi_{\alpha,(df=n-1)}{}^2$ of 16.92) at the probability level of 0.05. P3C@CaO–HCN nanocomposite material proved to be a suitable novel antimicrobial nanomaterial against *E. coli*, *P. aeruginosa*, and *C. albicans* pathogens in this work for the first time. The inhibition rates (I%) of 87.9%, 46.9%, and 72.5% were attained at MIC of 500 mg L^{-1} P3C@CaO–HCN for *E. coli*, *P. aeruginosa*, and *C. albicans*, respectively, due to damaging of the microbial membrane by the free cyanide (C≡N) functionality and protonated g-C_3N_4 (HCN) nanosheet. The notable high dyes adsorption capacities and antimicrobial activity by P3C@CaO–HCN offers its promising applications for industrial wastewater remediation and management.

References

1 V. S. Mane and P. V. V. Babu, *J. Taiwan Inst. Chem. Eng.*, 2013, **44**, 81–88.

2 C. Djilani, R. Zaghdoudi, F. Djazi, B. Bouchekima, A. Lallam, A. Modarressi and M. Rogalski, *J. Taiwan Inst. Chem. Eng.*, 2015, **53**, 112–121.
3 A. Duta and M. Visa, *J. Photochem. Photobiol., A*, 2015, **306**, 21–30.
4 K. P. Singh, S. Gupta, A. K. Singh and S. Sinha, *J. Hazard. Mater.*, 2011, **186**, 1462–1473.
5 N. A. Youssef, S. A. Shaban, F. A. Ibrahim and A. S. Mahmoud, *Egypt. J. Pet.*, 2016, **25**, 317–321.
6 E. Haque, J. W. Jun and S. H. Jhung, *J. Hazard. Mater.*, 2011, **185**, 507–511.
7 S. Li, *Bioresour. Technol.*, 2010, **101**, 2197–2202.
8 G. Z. Kyzas, A. Koltsakidou, S. G. Nanaki, D. N. Bikiaris and D. A. Lambropoulou, *Sci. Total Environ.*, 2015, **537**, 411–420.
9 J.-G. Yu, X.-H. Zhao, H. Yang, X.-H. Chen, Q. Yang, L.-Y. Yu, J.-H. Jiang and X.-Q. Chen, *Sci. Total Environ.*, 2014, **482**, 241–251.
10 Y. Jiang, J.-L. Gong, G.-M. Zeng, X.-M. Ou, Y.-N. Chang, C.-H. Deng, J. Zhang, H.-Y. Liu and S.-Y. Huang, *Int. J. Biol. Macromol.*, 2016, **82**, 702–710.
11 F. A. Al-Sagheer, E. I. Ibrahim and K. D. Khalil, *Eur. Polym. J.*, 2014, **58**, 164–172.
12 A. I. Hashem, W. S. I. Abou-Elmagd and A. Abd-Elaziz, *Eur. Chem. Bull.*, 2014, **3**, 1064–1068.
13 A. A. Oladipo, M. Gazi and E. Yilmaz, *Chem. Eng. Res. Des.*, 2015, **104**, 264–279.
14 R. Slimani, I. El Ouahabi, F. Abidi, M. El Haddad, A. Regti, M. R. Laamari, S. El Antri and S. Lazar, *J. Taiwan Inst. Chem. Eng.*, 2014, **45**, 1578–1587.
15 L. Pi, R. Jiang, W. Zhou, H. Zhu, W. Xiao, D. Wang and X. Mao, *Appl. Surf. Sci.*, 2015, **358**, 231–239.
16 G. Liu, X. Yang, T. Li, Y. She, S. Wang, J. Wang, M. Zhang, F. Jin, M. Jin and H. Shao, *Mater. Lett.*, 2015, **160**, 472–475.
17 W. Liu, M. Wang, C. Xu and S. Chen, *Chem. Eng. J.*, 2012, **209**, 386–393.
18 W.-J. Ong, L.-L. Tan, S.-P. Chai, S.-T. Yong and A. R. Mohamed, *Nano Energy*, 2015, **13**, 757–770.
19 J. Lützenkirchen, T. Preočanin, D. Kovačević, V. Tomišić, L. Lövgren and N. Kallay, *Croat. Chem. Acta*, 2012, **85**, 391–417.
20 P. Tripathi, V. C. Srivastava and A. Kumar, *Desalination*, 2009, **249**, 1273–1279.
21 S. A. Younis, N. S. El-Gendy, W. I. El-Azab, Y. M. Moustafa and A. I. Hashem, *Energy Sources, Part A*, 2014, **36**, 2566–2578.
22 M. Haerifar and S. Azizian, *J. Phys. Chem. C*, 2014, **118**, 1129–1134.
23 A. W. Marczewski, *Appl. Surf. Sci.*, 2010, **256**, 5145–5152.
24 N. Bakhtiari and S. Azizian, *J. Mol. Liq.*, 2015, **206**, 114–118.
25 P. S. Kumar, S. Ramalingam, C. Senthamarai, M. Niranjanaa, P. Vijayalakshmi and S. Sivanesan, *Desalination*, 2010, **261**, 52–60.
26 B. Tanhaei, A. Ayati, M. Lahtinen and M. Sillanpää, *Chem. Eng. J.*, 2015, **259**, 1–10.
27 M. Arshadi, F. S. Vahid, J. W. L. Salvacion and M. Soleymanzadeh, *Appl. Surf. Sci.*, 2013, **280**, 726–736.
28 J. R. Kim, B. Santiano, H. Kim and E. Kan, 2013.
29 M. Doğan, Y. Özdemir and M. Alkan, *Dyes Pigm.*, 2007, **75**, 701–713.
30 V. Vimonses, B. Jin and C. W. K. Chow, *J. Hazard. Mater.*, 2010, **177**, 420–427.